Int. J. Electrochem. Sci., 11 **(2016)** 1997 - 2017

International Journal of ELECTROCHEMICAL SCIENCE
www.electrochemsci.org

Preparation and Characterization of Nanomaterial Consisting of Silica Aerogel & Carbon Tested as an Electrode in Non-Aqueous Media Containing Lithium Salt

Anna Lisowska-Oleksiak[1,*], *Beata Wicikowska*[1], *Andrzej P. Nowak*[1], *Zbigniew Olejniczak*[2], *Czesław Kapusta*[3]

[1] Faculty of Chemistry, Department of Chemistry and Technology of Functional Materials, Gdańsk University of Technology, Narutowicza 11/12, 80-233 Gdańsk, Poland
[2] The Henryk Niewodniczański Institute of Nuclear Physics, Polish Academy of Sciences, Radzikowskiego 152, 31-342 Kraków, Poland
[3] AGH University of Science and Technology, Faculty of Physics and Applied Computer Science, Department of Solid State Physics, Al. Mickiewicza 30, 30-059 Kraków, Poland
[*]E-mail: alo@pg.gda.pl

Received: 23 November 2015 / *Accepted:* 15 December 2015 / *Published:* 1 February 2016

Silica aerogel (SiO_{2ag}) was combined with carbonaceous material in the pyrolysis process of hydrocarbons. The obtained nanocomposite SiO_{2ag}/C was amorphous, partially preserving the porous structure of SiO_{2ag}. The specific surface area changes from 445.6 m^2/g for pure SiO_{2ag} to 205.52 m^2/g SiO_{2ag}/C. The ^{29}Si MAS-NMR shows a three-dimensional matrix with silicon atoms connected to other silicon atoms by four and three oxygen bridges. The Raman spectrum reveals the state of carbonaceous material, with typical D and G peaks, derived from hydrocarbon pyrolysis. SiO_{2ag}/C was tested as an electrode in contact with $LiPF_6$ in the EC/DMC electrolyte. Electrochemical measurements showed the presence of complex redox couple activities of SiO_{2ag}/C. XPS was employed to identify products obtained under polarization of SiO_{2ag}/C. Silica reduction proceeds with Li_2O, $Li_2Si_2O_3$, $Li_2Si_2O_5$, Li_4SiO_4 and Li_xSi formation. The charge capacity after 30 cycles is equal to 550 mAh/g.

Keywords: silica aerogel, SiO_2@C, anode material, lithium – ion batteries

1. INTRODUCTION

An increasing demand for electrochemical energy storage and conversion devices stimulates progress in research on electrode and electrolyte materials. In the field of electrode materials silicon is the one of the most promising anode materials for Li-ion batteries (LIBs). However, silicon has a

drastic volume variation (around 3 times) during insertion and extraction of lithium ions [1–3]. There are hundreds of articles devoted to studies on silicon as an anode for lithium batteries. The review article by H. Wu *et. al.* is a comprehensive picture giving the state of the art in this field up to 2010 [4]. Interest nowadays is mainly focused on nanosilicon materials. However, a specific approach is undertaken. As an alternative, silica (SiO_2) has been considered to be the anode material of LIBs, because of the advantage of storing a large quantity of lithium and low discharge potentials [4,5]. Among literature data devoted to electrochemistry of SiO_2 one of the first of the most important is an article describing electrochemistry of a 400 nm thick film of pure silica without any binder [6]. Polarization curves taken in aprotic electrolyte (1.0 M $LiPF_6$ in EC/DMC 50/50 (v/v)) supported with XPS analyses, performed before and after polarization, brought about an explanation of the mechanism of the electrode reactions. It has been found that two mechanisms may occur separately or simultaneously. The first mechanism involves formation of silicate $Li_2Si_2O_5$ and Si (1) and Si alloying (2), both considered to be reversible reactions in Ref. [7]:

$$5\ SiO_2 + 4\ Li^+ + 4e^- \rightleftharpoons 2\ Li_2Si_2O_5 + Si \quad (1)$$

$$5\ Si + 22\ Li^+ + 22\ e^- \rightleftharpoons Li_{22}Si_5 \quad (2)$$

The second mechanism is less profitable as two reactions (3,5) are not reversible [7]:

$$2\ SiO_2 + 4\ Li^+ + 4\ e^- \rightarrow Li_4SiO_4 + Si \quad (3)$$

$$5\ Si + 22\ Li^+ + 22\ e^- \rightleftharpoons Li_{22}Si_5 \quad (4)$$

$$SiO_2 + 4\ Li^+ + 4\ e^- \rightarrow 2\ Li_2O + Si \quad (5)$$

Above electrochemical reactions of SiO_2 can be the source of a high theoretical capacity, significantly higher than capacity of LiC_6, as elemental silicon appears. However, pure silica is not conducting, thus a composition of appropriate structure, including empty space for alloying materials expansion, is desired. There are many literature examples of successful use of silica as an anode for lithium batteries [8-17]. Among them laboriously created hollow porous nanocubes are proposed [7]. Majority of studies on electrochemical activity of silica prove that only nanostructured SiO_2 is suitable for electrode application. In the case of a bulk crystalline form, milling is found to be very important. High energy mechanical milling was performed for crystalline silica (quartz) to obtain a successful stage of the material active under lithiation [9]. Two types of silicate were reported to be formed as a result of the cathodic reaction: lithium disilicate $Li_2Si_2O_5$ and lithium metasilicate Li_4SiO_4. It is worthy reminding here that both lithium salts are known to behave as fast ionic crystalline electrolytes [10,11]. Formation of disilicate, having a tunnel structure, is preferable, allowing reversible performance of the process [6,7,12].

In the latest reports on SiO_2 /C composite electrodes the main effort is made to obtain a nanostructure material using various methodologies. Silica mesoporous nanospheres with carbon porous shells are an example of a synergistic effect observed between components. A charge capacity above 600 mAh/g was recorded [13]. Similar results were obtained for nitrogen doped ordered mesoporous carbon/silica nanocomposites fabricated via the so called multi-constituent co-assembly strategy [14]. Chelation of the silicon cation led to formation of another type of SiO_2/C nanocomposite successfully tested as an anode for Li batteries [15]. Carbon thin films with SiO_x nanowires are an example of a different approach to the problem when partially reduced silicon oxides are used [16]. However, the charge capacity is relatively low (360 mAh/g).

In all recent studies mentioned above it is assumed that the electrochemical product of SiO_2@C reduction is based on lithium silicate formation accompanied by silicon lithiation as previously documented using ex situ XPS measurements [7] and SAEDTEM [17].

Here we use amorphous silica aerogel as a precursor of an anode material for LIBs. The used precursor is the most dispersed silica matter, easily available by simple synthesis at solvent critical conditions [18]. As received, the aerogel contains up to 95 % (vol.) of air. The very small particle size is achieved due to the synthesis route. The particle size is found to play a crucial role in electroactivity of SiO_2 [12]. In this work we focus on electrochemical performance of the material derived from silica aerogel combined with hard carbons formed during pyrolysis of hydrocarbons in the presence of silica aerogel.

2. EXPERIMENTAL

2.1. Material preparation

The anode material was derived from silica aerogel (density = 1,9 mg/cm^3). Silica aerogel (SiO_{2ag}) was prepared according to described methods in Ref. [18,19]. The specific surface area of obtained aerogels was analysed at 77 K according to the single-point Brunauer, Emmet & Teller (BET) method using the nitrogen absorption method as 445.6 m^2/g with an AREA Meter II (Ströhlein Instruments, Viersen, Germany).

The obtained material was impregnated with an aqueous solution of sucrose (POCH Gliwice) and sulphuric acid (POCH Gliwice). The concentration of sucrose was 1.5 M. After impregnation and decantation the material was treated with 0.6 M sulphuric acid. Then the gel was filtrated on a polypropylene (PP) drain, transferred into a ceramic corundum boat and pyrolysed using the programmable horizontal tube – furnace (Czylok, Poland) under a steady flow of argon atmosphere (30 cm^3/min) at 350ºC for 25 minutes followed by heating to 700ºC for 2 hours.

During the next step the material was powdered with glucose (POCH Gliwice) on an agate mortar and pestle to obtain uniform consistence. The silica aerogel/glucose weight ratio was 1:4. The powder was pressed on a manual hydraulic press (Specac Ltd.) for about 30 seconds with a load of 3.18 MPa on a 12 mm diameter matrix (Specac Ltd.). These pellets were pyrolysed under argon atmosphere with the same parameters as described above. This material is named by abbreviation SiO_{2ag}/C. EDX analysis gave the silicon to carbon atomic ratio of 1:8.

2.2. Materials characterization

The morphology of the sample was determined using a scanning electron microscope (SEM, Carl Zeiss AG, Germany) equipped with an EDX detector (EDS BRUKER AXS Quantax 200, Germany) and high-resolution transmission electron microscopy (HRTEM) measurements were carried out on a Tecnai F20 X-Twin TEM at 200 kV accelerating voltage.

The structure of the samples was measured by X-Ray diffraction (Xpert PRO - MPD Philips), Raman spectroscopy (Raman spectrometer in Via Renishaw, Renishaw, England), ATR FT-IR spectroscopy (Frontier spectrometer, Perkin-Elmer), solid state ^{29}Si Magic-Angle-Spinning Nuclear Magnetic Resonance (solid state ^{29}Si MAS-NMR) (Bruker HP WB) and X-ray Photoelectron Spectroscopy (XPS) (ESCALAB 250Xi, Thermo Fisher Science).

2.3. Measurement conditions

Raman spectra were recorded on a Raman spectrometer in Via Renishaw (Renishaw, England) with an Ar ion laser at a wavelength of 514 nm. Spectra were acquired over the range of 100 – 3200 cm^{-1} with a 2 cm^{-1} resolution. Depending on the signal intensity up to 10 spectra were accumulated to improve the signal/noise ratio and the total acquisition time did not exceed 5 min. The spectral analysis was performed with GRAMS/32 (Galactic) software. The spectra were analysed by the Lorentzian fitting procedure with 5 peaks. The goodness of fit χ^2 value was 1.33 and indicates that Lorentzian-shaped bands for 5 peaks are an acceptable value.

Solid state ^{29}Si Magic-Angle-Spinning Nuclear Magnetic Resonance (MAS-NMR) spectra were measured on the APOLLO console (Tecmag) at the magnetic field of 7.05 T produced by the 300 MHz / 89 mm superconducting magnet (Magnex). A Bruker HP-WB high-speed MAS probe equipped with a 4 mm zirconia rotor and KEL-F cap was used to spin the sample at 6 kHz. A single 3 μs rf pulse, corresponding to the π/2 flipping angle was used. The acquisition delay in accumulation was 60 s, and 512 scans were averaged. The frequency scale in ppm was referenced to the ^{29}Si resonance of tetra-methylsilane (TMS).

XPS measurements were carried out at base pressure of ~$1 \cdot 10^{-9}$ mbar. Al Kα monochromatized radiation (hν = 1486.6 eV) was employed as the X-ray source. Charge neutralization was implemented. Spectra were recorded with an energy step size of 0.1 eV at a pass energy of 15 eV for highly resolved C 1s, O 1s and Si 2p peaks. The binding energies were corrected by setting the C 1s hydrocarbon (–CH_2–CH_2–bonds) peak at 285.0 eV for graphite electrodes. Ar^+ etching was performed for 2000 s for depth profile analysis. The data processing (peak fitting) was calculated with Avantage software provided by Thermo Fisher Scientific, using Smart type background subtraction and Gaussian/Lorentzian peak shapes.

2.4. Electrochemical measurements

The electrochemical behaviour of the samples was examined using two- and three – electrode Swagelok® type cells vs. Li (lithium foil 99.99% purity, 0.75 mm thickness, AlfaAesar) with 1 M $LiPF_6$ dissolved in an ethylene carbonate (EC) and dimethyl carbonate (DMC) mixed solvent (LP30 Merck, Germany) as the electrolyte. The working electrode was prepared from SiO_{2ag}/C material with polyvinylidene fluoride (PVDF, Solvay S.A., 5 % wt.) as binder dissolved in *N*-Methyl-2-pyrrolidone (NMP, Sigma - Aldrich) using an ultrasonic bath for 3 hours. The SiO_{2ag}/C material was in the form of a slurry for film fabrication on copper foil (Schlenk Metallfolien GmbH & Co KG, Germany).

Obtained disc-shaped electrodes were dried under dynamic vacuum in an oven (Glass Oven B 585 Büchi, Germany) for 24 h at 80 ºC. The cells, equipped with a SiO_{2ag}/C working electrode, lithium disc as the counter electrode with lithium wire as reference electrode, were assembled in an argon-filled Lab Star glove-box workstation (MBraun). For battery tests electrochemical measurements were performed in two electrode Swagelok® type cells with active material as the working electrode and lithium foil (99.9% purity, 0.75mm thickness, AlfaAesar, Germany) as the counter/reference electrode.

The oxygen and water level in the glove box were maintained below 0.5 ppm.

Cyclic voltammetry was performed using an electrochemical potentiostat/galvanostat Autolab (PGStat302N, The Netherlands) between 0.01 (±0.004) – 2.7 (±0.004) V versus Li/Li^+ at a scan rate of 100 $\mu V \cdot s^{-1}$. All measurements were performed at 21 (±1) ^oC.

After the charging (E=0.01 V, Q=3295 C/g) procedure the cell was disassembled in the argon-filled glove box and the working electrodes were taken out from the cell, washed with propylene carbonate (PC, Sigma-Aldrich), then dried at 60 ^oC under dynamic vacuum for 24 h for XPS characterization. Dried and encapsulated samples were transferred to the XPS chamber with great care using a glove bag (Sigma - Aldrich) purged with Ar 5.0.

The discharged material taken for XPS measurements came from multicyclic polarization described in section 3.3.

The equilibrated rest potential for the charged material was E_{rest}=0.2 V. The rest potential after discharging was E_{rest}=3.2 V.

Galvanostatic cyclic polarization tests were performed with a multichannel battery interface ATLAS – SOLLICH 0961 MBI (Poland). The cells were cycled between 0.01 and 3.0 V versus Li^+/Li at a current density of 18 mA/g.

3. RESULTS AND DISCUSSION

3.1. Morphology

Scanning electron microscopy was applied to study morphology of the materials.

Images of pure silica aerogel and SiO_{2ag}/C are presented in Fig. 1 a, b and Fig. 1 c, d, respectively.

The silica aerogels with typical interconnected porous network have a well-developed three-dimensional structure as described in Ref. [20], see Fig. 1. a, b. It can be observed that the structure of the aerogel is highly cross-linked. Silica aerogels contain closely bound and almost monodispersed spherical particles with polydispersed porosity.

In Fig 1. c, d the obtained SiO_{2ag}/C material is shown. The material is more compact in comparison with pure silica aerogel. Silica is sheltered by uniformly spread hard carbon coming from pyrolysed glucose. The absence of an open pore silica network is caused by a high temperature process. However, one may see that the porous cross-linked network of the aerogel is partially preserved, see Fig. 1 d. The specific surface area changes from 445.6 m^2/g for SiO_{2ag} to 205.52 m^2/g for SiO_{2ag}/C. The total pore volume diminishes from 0.17 cm^3/g for SiO_{2ag} to 0.11 cm^3/g for SiO_{2ag}/C.

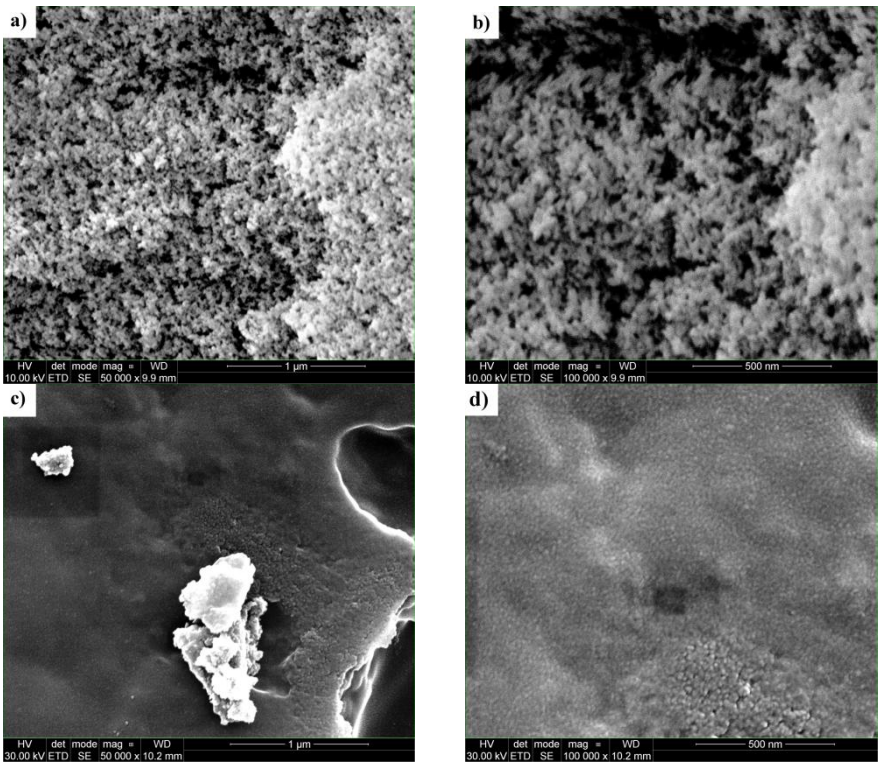

Figure 1. SEM images of a)-b) pure silica aerogel, c)-d) pyrolysed SiO_{2ag}/C material

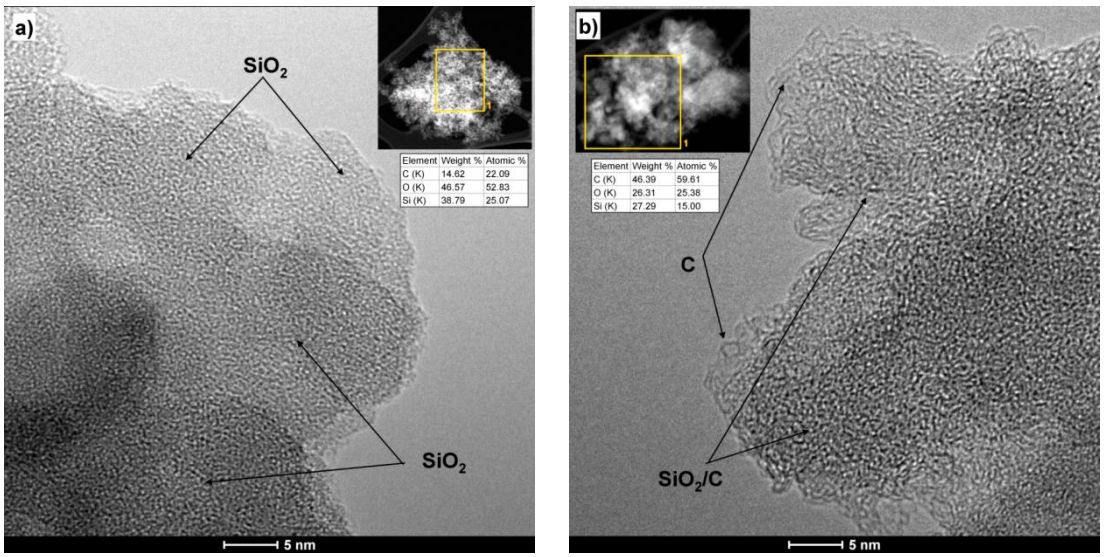

Figure 2. HRTEM images of a) silica aerogel and (b) carbon coated silica aerogel.

The HRTEM images of the SiO_{2ag} and the SiO_{2ag}/C materials illustrating the shape and particle size are shown in Fig. 2. The dark and white areas on HRTEM photos are attributed to the bulk material and pores in both materials. The micrograph of pure SiO_{2ag} is typical for an amorphous material of meshwork structure. The morphology of the SiO_{2ag}/C material is similar to pure aerogel. The carbon structure in carbon coated silica aerogel is typical as that observed for amorphous and

disordered carbons [21]. This is expected as the pyrolysis temperature (700°C) was not sufficient to form a graphitic structure [22]. The amorphous phase of carbon is visible at the edges of the material (Fig. 2b) in the form of layers of non-defined structure.

In the inset in Fig 2 the EDX analysis is shown. The results clearly indicate that SiO_{2ag}/C is covered with carbon (~ 59 % at.) originating from pyrolysed glucose while SiO_{2ag} is pure silica. The carbon amount in Fig. 2a is due to the presence of impurities adsorbed at the silica surface. These results are in agreement with data obtained by SEM analysis.

3.2. Structural Characterization

Structural characterization of SiO_{2ag}/C was performed using: X-Ray analysis, ATR-FTiR spectroscopy, Raman spectroscopy, Si-MAS NMR and XPS spectroscopy.

3.2.1. X-Ray Diffraction

The XRD pattern of the SiO_{2ag}/C material is shown in Fig. 3.

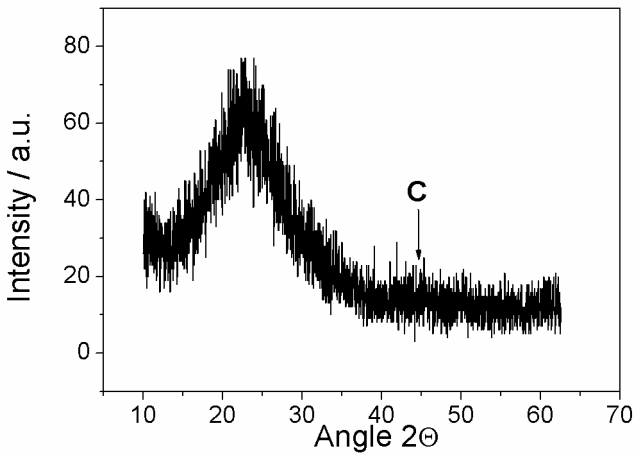

Figure 3. XRD pattern of pyrolysed SiO_{2ag}/C material.

The X ray diffraction pattern proves the amorphous character of the composites with only one broad peak measured at the low angle (2 theta). Wide peaks at about 22° and 44° are attributed to SiO_2 nanoparticles and the amorphous carbon structure, respectively. Similar results are reported in Ref. [8]. There is no peak of elemental crystalline silicon. This confirms that SiO_2 was not reduced to Si as one may expect and it is in agreement with earlier reported literature data that SiO_2 cannot be reduced to glass-like compounds by carbon at 1000° C [17,23].

3.2.2. Attenuated Total Reflectance Fourier Transform Infra Red Spectroscopy (ATR-FTIR)

The ATR-FTIR spectrum of the SiO_{2ag}/C material is shown in Fig. 4.

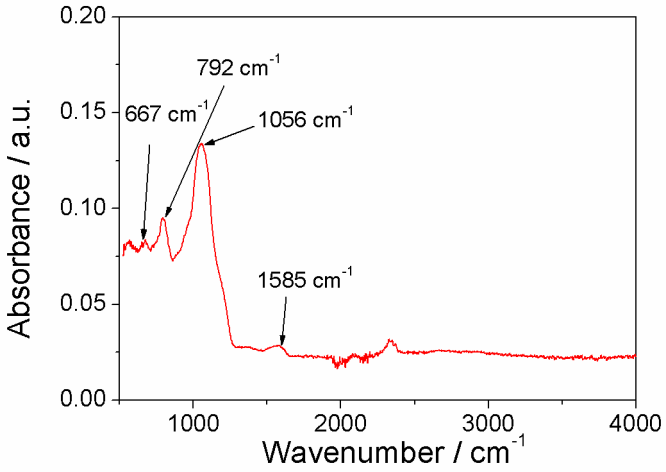

Figure 4. The ATR-FTIR spectrum of pyrolysed SiO2ag/C material

The peaks at 1056, 792 cm^{-1} are assigned to the asymmetry Si–O–Si bond stretching vibration [7]. These two characteristic peaks confirm the presence of SiO_2. The maxima in the wavenumber region below 1000 cm^{-1}, known as the fingerprint region, come from stretching and deformation vibrations which may confirm Si-C bond formation in the sample (667 cm^{-1}) [24]. The intensity of silicon carbide signals is rather low and no proof for the SiC crystalline form is found on the XRD pattern. The maximum seen at ~ 1585 cm^{-1} may be ascribed to vinyl groups bonded to silicon [25].

3.2.3. Raman Spectroscopy

Micro-Raman-spectroscopy was applied to determine the structure of carbon from SiO_{2ag}/C in the samples. The shape of the presented Raman spectrum, (Fig. 5) is typical for disordered carbonaceous material where two quite sharp modes, the D peak around 1356 cm^{-1} and the G peak around 1595cm^{-1} are recorded [26]. Similar values for D and G bands around 1360 cm^{-1} and 1590 cm^{-1} were reported by Maier *et.al.* for the nanocomposite formed as a core shell structure Si@SiO_x/C, where glucose was the carbon precursor, used during the hydrothermal carbonization process [27]. The *D* peak is attributed to the disorder-induced vibration mode of graphene layers in the carbon phase, linked to the breathing motion of sp^2-rings. The *G* line may even be attributed to sp^2 stretch vibrations of carbon atoms [28]. It is known that interpretation of Raman spectra in the range 1000 -2000 cm^{-1} should be performed with five bands [29]. These bands are: D2, D, D3, G and D4. The D2, D and D4 bands are attributed to a disordered graphitic lattice, the G band confirms the presence of an ideal graphitic lattice, while the D3 band originates from an amorphous carbon phase [30,31]. The spectrum was deconvoluted into 5 peaks with Lorentzian fitting according to the procedure given in Ref. [29].

The maxima of D2, D, D3, G and D4 bands have been recorded at 1222, 1351, 1488, 1579 and 1608 cm^{-1}.

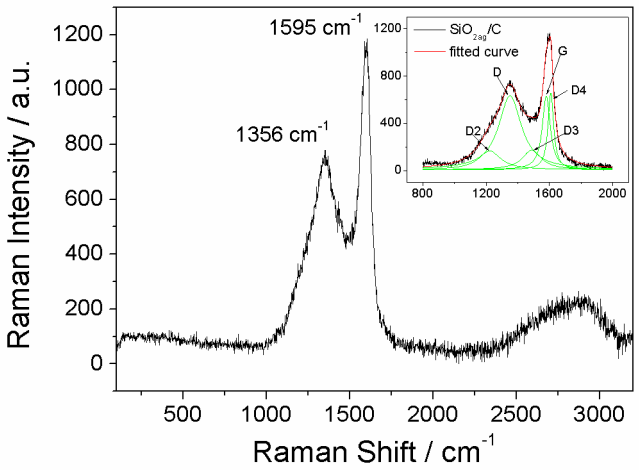

Figure 5. Raman spectrum of pyrolysed SiO_{2ag}/C material, *inset*: The curve fit for first order Raman spectra of SiO_{2ag}/C.

The intensities of the two lines (*D* and *G*) depend on the type of graphitic material. It is known that the ratio of intensities *I(D)* to *I(G)* varied inversely with L_a for carbonaceous materials according to the equation given in Ref. [26]:

$$\frac{I(D)}{I(G)} = \frac{C(\lambda)}{L_a} \quad (6)$$

where *C* depends on the Raman laser excitation energy (for λ = 514.5 nm, *C* = 44 Å) and *I*(*D*)/*I*(*G*) is the peak height ratio.

The intensity of *I(D)/I(G)* proposed by Tuinstra and Koenig [26] was used to evaluate the carbon cluster size. Authors studied the relationship between the ratio measured from the Raman spectrum and the graphitic in-plane microcrystallite size, L_a.

The *I(D)/I(G)* peak height ratio for SiO_{2ag}/C material equals 1.00, so the L_a parameter is estimated at 44 Å. Tuinstra and König have observed that when the value of the *I(D)/I(G)* ratio is ~1.0, it may be ascribed to uniformly monocrystalline forms of graphite [26]**.** For a system with a mixed grain sizes one should calculate an effective L_a parameter as is shown in Ref. [28]**.**

3.2.4. ^{29}Si MAS-NMR

The ^{29}Si MAS-NMR spectra of the pristine SiO_{2ag} and the sample after pyrolysis with the carbon precursors (SiO_{2ag}/C) are shown in the top and bottom of Fig. 6, respectively (black dots). The red lines represent the fits to the spectra, consisting of two Gaussians located at -110 and -101 ppm, with relative contributions of 70 and 30 %. The FWHH values are equal to 8.6 and 10.9 ppm for the

SiO_2 and SiO_2/C spectra, respectively. The slight increase of the linewidths can be due to the pyrolysis process.

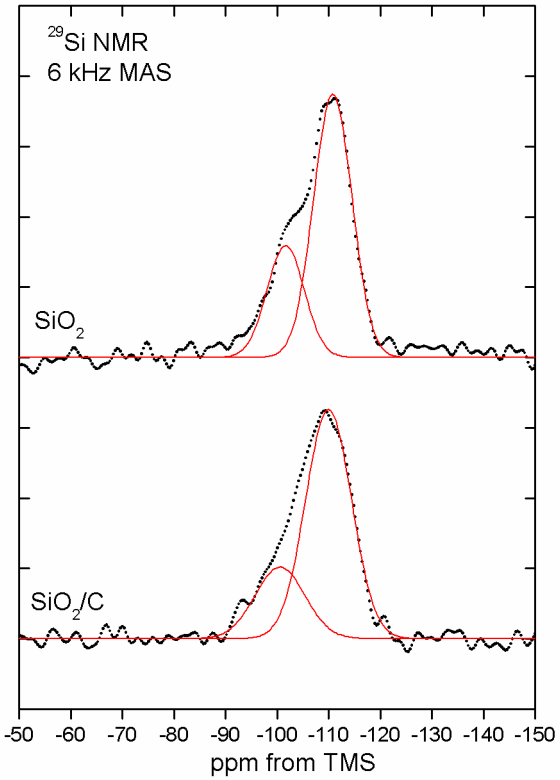

Figure 6. ^{29}Si NMR spectra of pristine SiO_{2ag} and SiO_{2ag}/C materials.

The line at -110 ppm is typical for bulk silica, corresponding to tetrahedrally coordinated silicon atoms, which are connected to other silicon atoms by four oxygen bridges (Q^4 units), forming a three-dimensional matrix. The line at -101 ppm can be assigned to Q^3 units, with three oxygen bridges, which may correspond to silicon atoms located close to the surface of silica particles [32].

Spectra show that the pyrolysis process did not affect the structure of the silica aerogel matrix, apart from introducing a slightly bigger disorder, as evidenced by increased linewidths. On the other hand, any lines that would correspond to Si-C or Si-O-C bonds and would appear at higher field, in the 5-65 ppm range [33,34], are not observed. Similarly, no reduced form of silicon as Si-C-O glass-like compounds was reported for nano-silica in hard carbon studied by Guo *et al.* [17].

3.2.5. X-ray Photoelectron Spectroscopy (XPS)

XPS spectra for the SiO_{2ag}/C electrode material are presented in Fig. 7-9.

Fig. 7 shows spectra for pristine material, Fig. 8 for charged material (E_{rest} = 0.2 V) and Fig. 9 for discharged material (E_{rest} = 3.2 V).

3.2.5.1. Pristine Material

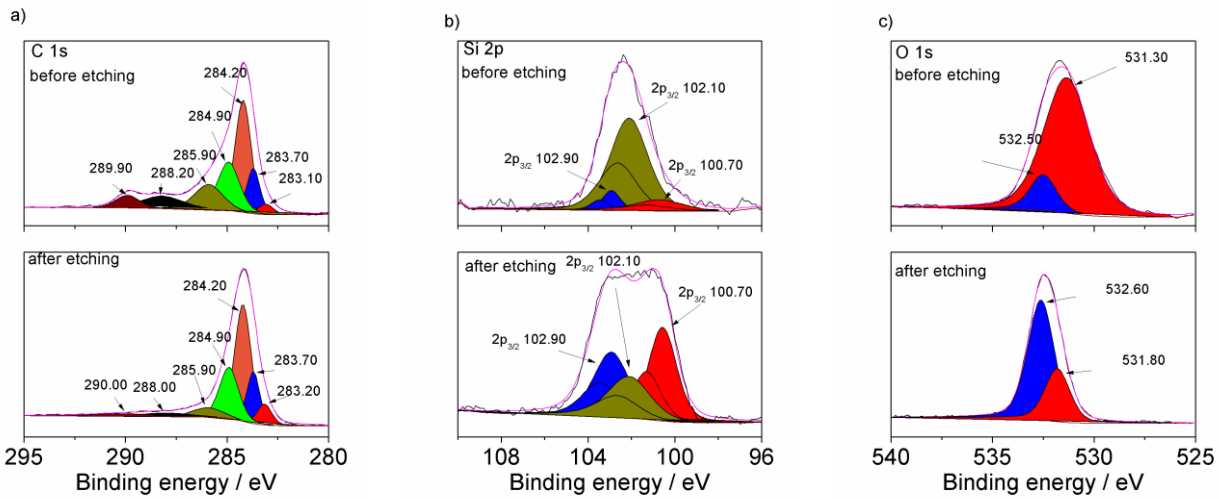

Figure 7. XPS spectra of pristine SiO_{2ag}/C electrode material of a) C 1s, b) Si 2p and c) O 1s core level before and after Ar^+ etching

The XPS spectra of a) C 1s, b) Si 2p and c) O 1s core level of pristine material before and after the Ar^+ etching procedure are shown in Fig. 7.

The C 1s core level identifies the presence of a few types of carbon compounds, see Fig. 6a. The fitting procedure gives peaks at 283.10 eV (C-Si bond) [24,35], 283.70 (C-Si bond) [36], 284.20 eV (graphite or C=C bond) [37], 284.90 (C-H bond) [38–41], 285.90 eV (C-O bond) [42], 288.20 eV (C-H or C-O bonds) [37,40] and 289.90 eV (C-F or -CO_3 bonds) [39–41]. The first two peaks correspond to silicon carbide or silicon oxycarbide which are formed during the pyrolysis procedure. The intensity of the carbon peak corresponding to carboxyl and carbonate groups diminishes after Ar^+ etching (Fig 7 a.).

Deconvolution of the Si 2p spectrum into three components is shown in Fig. 7 b.

The first doublet ($2p_{3/2}$ and $2p_{1/2}$), located at 100.70 and 101.30 eV might correspond to the Si-C bond [43]. However, the ^{29}Si NMR spectrum, see Fig. 6, did not confirm presence of Si-C or Si-O-C bonds which would appear in the -5 - 65 ppm range [33,34]. Similarly, Guo *et al.* did not observe these bonds in nano-SiO_2 in the hard carbon anode material [17]. Thus, the BE 100.70 eV is very likely to originate from disordered $SiO_{x-\delta}$ with Si atoms at lower valence.

The second pair, located at 102.10 and 102.60 eV, is attributed to Si-O coming from SiO_x or SiOC [42,44]. The component seen at the highest binding energy (102.90 and 103.50 eV) is known to be associated with SiO_2 and/or silicon oxycarbide formation [35]. No shifts in binding energy were recorded for the sputters (Ar^+) sample, see Fig. 7 b.

In the spectra of O 1s shown in Fig. 7 c one peak at 531.34 eV was assigned to the C -O bond [45]. The second peak is located at 532.50 eV and originates from bonding Si-O in SiO_2 [42]. The position of this peak is slightly (0.1 eV) shifted towards higher binding energy (532.60 eV) in a sample after Ar^+ sputtering. The intensity of this peak increased significantly after the etching procedure. The peak seen at 531.30 eV vanishes after Ar^+ sputtering, while a peak at 531.80 eV appears. The binding energy at 531.80 eV can be prescribed to the Si-O bond from SiO_x species [46].

3.2.5.2. Charged Material

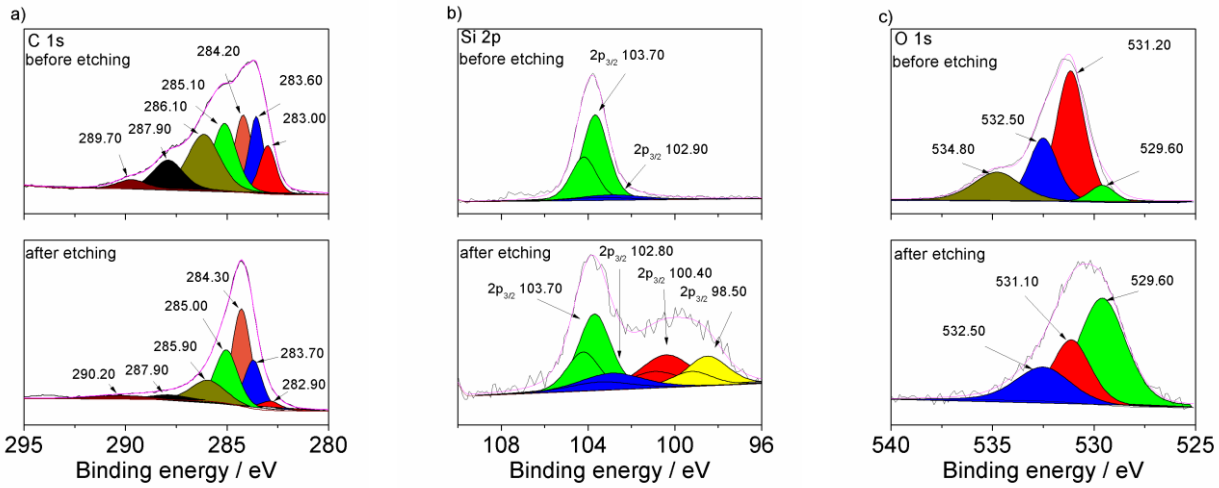

Figure 8. XPS spectra of charged SiO_{2ag}/C electrode material of a) C 1s, b) Si 2p and c) O 1s core level before and after Ar+ etching

The XPS spectra of C 1s core level for the charged material (see Fig. 8 a) exhibit the peak position at similar binding energy (± 0.3 eV) as it is observed for charged material (polarized at 0.2V shown in Fig. 7 a.)

In the Si 2p core level two forms can be identified. The first is located at 102.90 eV ($2p_{3/2}$) and the second is at 103.70 eV ($2p_{3/2}$), see Fig. 8 b. The latter is ascribed to the Si-O bond in Li_2SiO_3 [47] while the former is attributed to $Li_2Si_2O_5$ [6]. The Si 2p spectrum, deconvoluted from Fig 8 b, gives four multiplets corresponding to split $2p_{3/2}$ and $2p_{1/2}$ core holes. These peaks (2 $p_{3/2}$) are located at 98.50 eV, 100.40 eV, 102.80 eV and 103.70 eV. The first (98.5 eV) is very likely to be attributed to the Li-Si bond in Li_xSi alloy. Recently Edström *et al.* showed that the peak localized below 98 eV can be ascribed to the Li_xSi alloy, whereas the BE value at 100.40 eV may be attributed to the Si-O bond coming from silicate Li_4SiO_4 [41]. The last two peaks seen at 102.80 and 103.70 eV are very likely to be attributed to the Si-O bond present in Li_2SiO_3 [47] and $Li_2Si_2O_5$ [6].

In Fig. 8 c. the O 1s signal is fitted with four peaks at 529.60, 531.20, 532.50 and 534.80 eV. These peaks are attributed to the Li-O bond, C-O bond, Si-O bond and CF-O bond, respectively. The peak present at 529.60 eV can be assigned to Li_2O formed during the electroreduction process [48]. The compound formed at 531.20 is very likely to originate from Li_2CO_3 formation on the surface

[42,44]. The maximum seen at 532.50 eV confirms the presence of SiO_2 [42,46] or/and $Li_2Si_2O_3$/$Li_2Si_2O_5$ [42]. The Si-O binding energy originating from silicates $Li_2Si_2O_3$/$Li_2Si_2O_5$ overlaps and is difficult to be distinguished as is claimed by Osaka *et. al*.[42]. The peak recorded at the highest binding energy can be ascribed to a compound like organic-fluorinated and/or organofluoro-phosphorous coming from degradation of the $LiPF_6$ electrolyte [39,48]. Disappearance of the peak at 534.80 eV after Ar^+ etching proves that the outer layer of the solid electrolyte interphase (SEI) was removed, see Fig. 8 c.

3.2.5.3. Discharged Material

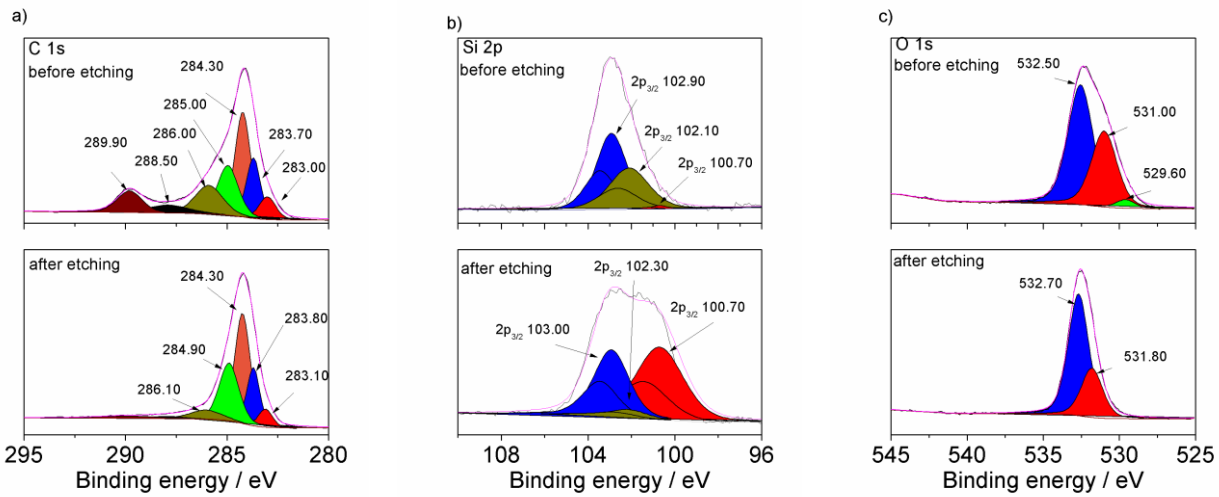

Figure 9. XPS spectra of discharged SiO_{2ag}/C electrode material of a) C 1s, b) Si 2p and c) O 1s core level before and after Ar+ etching

The XPS spectra of C 1s core level for discharged material, see Fig. 9 a., maintain location at a similar binding energy (± 0.3 eV) as is observed for the charged material (Fig. 8 a).

In the spectra of Si 2p shown in Fig. 9 b. two doublets are detected, the first localized at 102.10 eV ($2p_{3/2}$) and the second seen at 102.90 eV ($2p_{3/2}$). Both of them are ascribed to Si-O bonds in different compounds consisting Si and O atoms. The former originates from SiO_x [42,49] or Li_4SiO_4 orthosilicate [17]. The peak at 102.10 eV vanishes due to sputtering, while the peak at 100.70 eV appears. The maximum localized at lower BE (100.70 eV) is ascribed to more disordered $SiO_{x-\delta}$ as is observed for the pristine material, see Fig. 7 b.

Deconvolution of O 1s spectra is shown in Fig. 8 c. The maxima are recorded at 529.80, 531.00 and 532.50 eV for discharged material before Ar^+ etching and at binding energies of 531.80 and 532.70 eV after Ar^+ ion sputtering. The signals at 529.80 and 531.0 eV are very likely attributed to Li_2O and $Li_2Si_2O_3$ compounds [42,48]. The maximum at 532.5 eV may be assigned to SiO_2 [42,46].

Table 1 shows gathered information about supposed chemical compounds of the studied material concerning only the results obtained for the etched sample. It is noteworthy that the polarized material is covered by chemicals typical for SEI formed in the electrolyte containing $LiPF_6$ salt.

Table 1. Chemical compounds identified in the studied material.

Pristine material	Charged material (E_{rest}=0.2 V)	Discharged material (E_{rest}=3.2 V)
SiO_2, SiO_x, $SiO_{x-\delta}$, C	SiO_2, C, $Li_2Si_2O_3$, $Li_2Si_2O_5$, Li_4SiO_4, Li_xSi, Li_2O, Li_2CO_3,	SiO_2, SiO_x (negligible signal), $SiO_{x-\delta}$, C

3.3. Electrochemical Characterization

The electrochemical cell Li|1M $LiPF_6$, EC,DMC|SiO_{2ag}/C was prepared using T-shape Swagelok® without separator. In Fig. 10. CV curves obtained at a sweep rate of 100 μV/s for material SiO_{2ag}/C are shown.

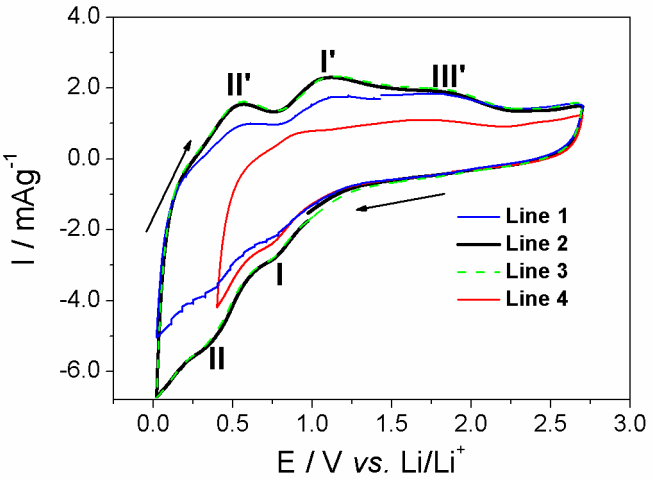

Figure 10. Cyclic voltammogram of SiO_{2ag}/C electrode material, sweep rate v = 100 μV/s, potential range: 0.02 – 2.7 V.

Before CV measurements the sample was potentiostatically polarized at *E* = 0.02 V as the charge reached a value of Q=2.62 C (8733 C/g)**.** The first CV scan was started at a rest potential of 1.5 V and the sample was polarised anodically to a limiting potential of 2.7 V. Then the potential was reversed cathodically and swept up to 0.01 V (see Line 1). Two cathodic current waves with a plateau marked at 0.8 (I) and 0.37 V (II) are observed. The anodic current peaks at 0.55 V (II'), 1.11 V (I') and 1.86 V (III') are recorded on the reverse branch of the cv curve. To distinguish which maxima originate from the redox couple, the CV curve of lower cathodic limit was recorded, see line 4. Comparing both, line 1 and line 4, one can see that the anodic peak at 0.55 V is in response to a

cathodic maximum marked 0.37 V. The next redox couple activity is seen as a cathodic current growth marked 0.8 V with an anodic hump at 1.11 V followed by a broad plateau (marked 1.86 V).

In order to enhance electrochemical restructuring of the SiO_{2ag}/C film another cathodic potentiostatic polarization was performed. The next step in the experiment involved two subsequent CV cycles (line 2 and 3). As can be seen, they overlap each other, proving reproducibility of the process. Thus, the performed charging /discharging procedure caused phase changes in the bulk of material. This is in contradiction to other reports, showing a non-reproducible, singular polarization curve. It is impossible to analyse the redox potential as no define phases were formed as literally indicated in Ref. [50]. Analysing XPS results one may conclude that silica undergoing reduction observed as a current growth (0.80 V) brings about products active in the second stage of the cathodic process (0.37 V). The reaction fulfilling these requirements is production of silicate and silicon. Such a reaction may proceed according to equations 1 and/or 3, see Introduction. Moreover, another process in which silica and also SiO_x participate may be considered as:

$$SiO_2 + SiO_x + z\,Li^+ + z\,e^- = Li_{(z-2)}SiO_{(x+1)} + Li_2O + Si \quad (7)$$

A similar reaction was proposed by Doh *et. al.* [50]. Lithium oxide was detected in the charged sample. Also elemental silicon was not identified by XPS, the presence of lithium silicate is confirmed, see Table 1.

Thus, considering equations 1, 3 and 6 the reduction products are: Li_2O, Li_xSiO_y (Li_4SiO_4, $Li_2Si_2O_5$) and Si. Silicon obtained is very likely to uptake lithium during alloying marked at 0.37 V to form Li_xSi, see Fig. 10.

On the anodic branch of the CV curve the maximum at 0.55 V results from dealloying of Li_xSi, as was already reported for Si derivative composites [50]. The peak at 1.11 V may be ascribed to a reversible reaction in which silica is produced from silicates and Li^+ ions are released, see eq. 1, 3 and 7. SiO_x species are not identified by XPS for discharged samples, though. However, it should be noted that reaction 3 is described as an irreversible one [7], whereas in the studied case the CV is reproducible as was found by other authors [17]. Thus, the simplified schematic and summarizing representation of the process may be given as:

$$Li_xSiO_y + Li_2O + \frac{y-1}{2}Si = \frac{y+1}{2}SiO_2 + (x+2)Li^+ + (x+2)e^- \quad (8)$$

The hump at 1.1 V opens a long plateau reaching minimum current values at potential 2.1 V. A similar plateau was observed by Sun *et al.* (see, eq. 1), who ascribed it to the electrochemical activity of $Li_2Si_2O_5$ in a reaction leading to formation of SiO_2 [6]. Thus, a part of Li_xSiO_y from eq. 8 may be attributed to disilicate $Li_2Si_2O_5$.

The current growth observed at a more negative potential than 0.2 V originates from both silicon and carbon lithiation [51]. CV polarization allows to conclude that silicon is dispersed inside the material in the desired manner very likely allowing secure volume expansion.

The galvanostatic charge and discharge of SiO_{2ag}/C at a different ratio of Si:C (1:3 and 1:8) were evaluated at a current density of 18 mA/g between 0.01 and 3.0 V vs. Li^+/Li. The specific capacity was calculated based on active SiO_2 in the electrode material. Hard carbon participation in the specific capacity was acknowledged as being equal to 30 mAh/g, as reported by Dahn [52].

Authors proved that hard carbons obtained from hydrocarbons during pyrolysis under argon demonstrated a dramatic reduction of irreversible capacity [52].

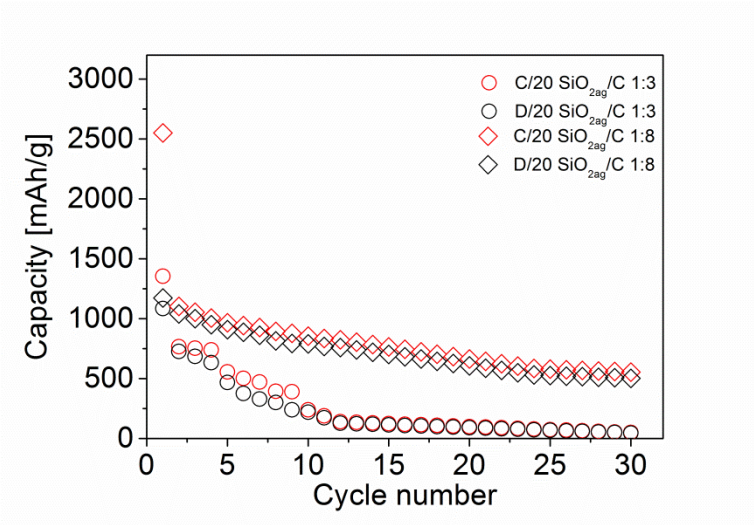

Figure 11. Capacity vs. cycle number of different Si:C materials at C/20

As shown in Fig. 11, the first cycle discharge and charge capacities of the SiO_{2ag}/C [1:8 at. %] electrode reached values of 1172 and 2562 mAh/g, respectively. The discharge capacity is much higher than the theoretical capacity of pure silica which is 1965 mAh/g [7], although a big capacity loss of 70% occurred in the first cycle because of SEI film formation. After 30 charge–discharge cycles, the discharge capacity still remained at up to 550 mAh/g. However, the obtained values are lower than the theoretical specific capacity of silica.

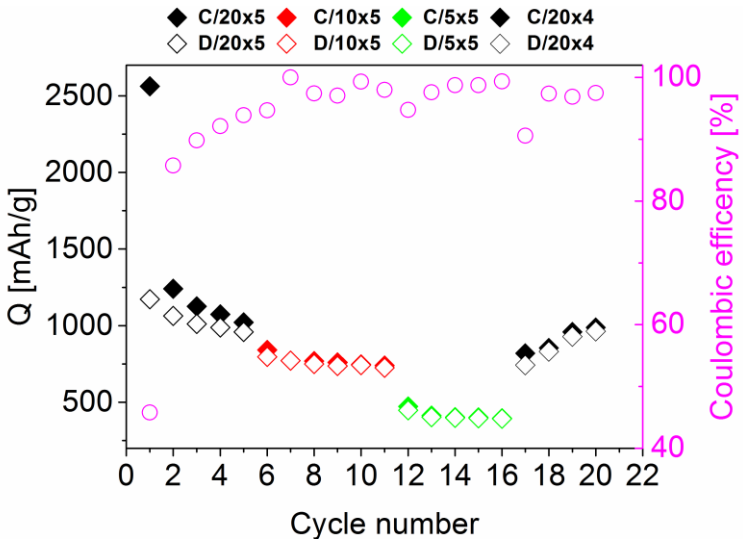

Figure 12. Capacity vs. cycle number of Si:C 1:8 material at different C – rates

In Fig. 12 the capacity for SiO_{2ag}/C 1:8 material at different charging/discharging rates (C20, C10. C5) was shown. As can be seen, the charge capacity drops for fast charging, while the whole material reaches good capacity again after a cycle under lower current density.. The reason of such behaviour is related to slow kinetics and diffusion of studied processes.

Table 2. Specific capacity data compared with the literature.

Material	Number of cycles	Capacity [mAh/g] (scan rate or current density)	Ref.
SiO_{2ag}/C	30	550 (18.6 mA/g)	
C/SiO_x NWs	30	360 (0.1 C)	[16]
SiO_2-carbon composite	100	662- 602 (C/10)	[15]
DMSNs/C	200	635 (100 mA/g)	[13]
N-OMC/ SiO_2	100	876 (200 mA/g)	[14]
SiO_2@C@graphene composite	200	250 (50 mA/g)	[53]
RAD	80	500 (18.6 mA/g)	[54]
SiO_2@C	103	500 (0.2 mA/cm^2)	[55]
SiO_x/C composite	350	780 (100 mA/g)	[56]
SiO_xC_y	1000	1020 (1C)	[57]
Hollow porous SiO_2 nanocubes	30	919 (100 mA/g)	[7]
Amorphous Si/ SiO_x/ SiO_2 nanocomposites	350	600 (200 mA/g)	[58]
Quartz (SiO_2)	100	800 (100 mA/g)	[12]
$SiO_{1.3}$	200	1058-930 (1924 mA/g)	[9]
C-SiO_2	50	536 (50 mA/g)	[8]
Si-O-C	50	600 (?)	[59]
SiO_2 thin film	100	510 (0.028 mA/cm^2)	[6]
Si@ SiO_x/C	60	1100 (150 mA/g)	[27]
Nano- SiO_2	15	1675 (0.1 mA/g)	[17]

Table 2 presents a list of battery parameters of different SiO_x anode concepts, reported in Ref. [6–9,12-16,17,27,54–58,60,62]. The Authors report that the capacity has been calculated only in respect to the active material presence in the whole composite [13]. This approximate value for the capacity of the electrode should be even smaller, considering the amount of the conductive additives and binders of the slurry. However, taking into account other capacity values, where authors do not report how they calculate the capacity, our anode material exhibits specific capacity at the same level. Besides considering the capacity and the charging rate when comparing electrodes, it is also important to take a look at voltage limits taken for battery cycling. In Ref. [12,27,57,58] authors presented their experiments in narrower potential ranges than 3.0 – 0.01 V. Therefore, intentionally, the process is limited to silicate and silica formation, avoiding alloying and all the difficulties over pulverization.

In current studies SiO_{2ag}/C is polarized up to Li_xSi_y alloy formation and the system was found to be mechanically stable as the growth of capacity is observed (see Fig.12). The charge density of the used SiO_{2ag}/C anode is comparable to other anodes reported in literature (see Table 2).

The impedance spectra of pristine (E = 3.0 V) and charged (E = 0.2 V) materials are shown in Fig. 13.

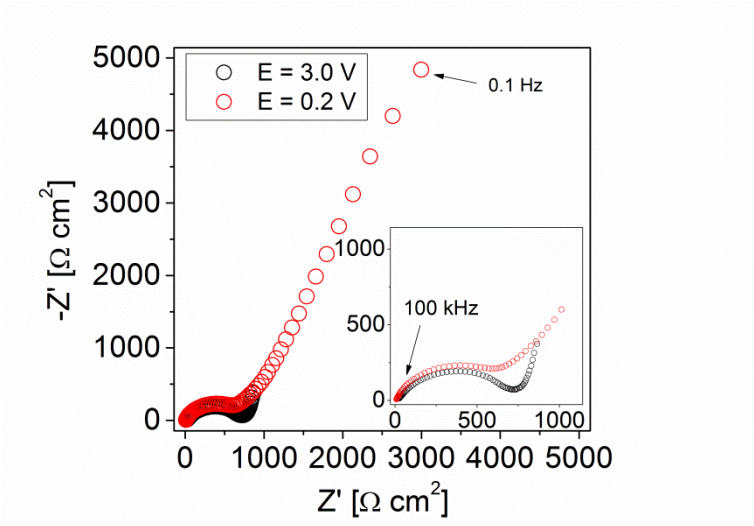

Figure 13. Nyquist plots of SiO_{2ag}/C electrode (Ø = 6 mm, thickness 50 μm) at E = 3.0 V (o) and E = 0.2 V (o).

Both spectra consist depressed semicircles followed by a sloping line at lower frequencies. The slope of the line for an electrode material at E = 3.0 V, rising at an angle of 80° to the Z' axis typical for capacitive impedance with *CPE* character. For the charged electrode, E = 0.2 V, the straight line in the low frequency region is inclined at an angle of 60° to the real axis. It suggests that diffusion in the bulk is a process consisting of finite-length Warburg diffusion with reflective boundary conditions. Taking into account inhomogeneity of the film the Warburg impedance should be identified by the generalized finite-length Warburg element (GFW) [61,62].

4. CONCLUSIONS

Amorphous silica aerogel was successfully combined with carbonaceous conductors during pyrolysis of hydrocarbons. In this work we exhibit electrochemical behaviour of SiO_{2ag}/C 1:8 material. Our results demonstrate that tested nanocomposite material is electroactive at high negative potential range, however its utilization in energy storage devices would be limited to low charge/discharge rates.

Electrodes and material has been characterized in respect to its structure, morphology and electrochemical activity by means techniques of as described below. The XRD measurements confirmed the presence of a non-crystalline carbon phase in the studied material. Infrared spectroscopy

evidenced SiO_2, while Raman spectroscopy indicated maxima originating from disordered and graphitized carbon. ^{29}Si MAS-NMR spectra of SiO_{2ag}/C excluded Si-C bond formation during material preparation. This is in agreement with SEM and HRTEM results which evidenced that silica was sheltered by uniformly spread hard carbon. Pyrolytic coverage of SiO_{2ag} nano-net by the carbonaceous film is found to be vital to attain SiO_{2ag} electroactivity.

XPS measurements confirmed the reversible electrochemical reduction of silica aerogel to lithium silicates and lithium silicide. Two couples of reduction and oxidation peaks at 0.8 V/ 1.11 V and 0.37 V/ 0.55 V were found on CV polarization curves. The former was attributed to silica reduction with lithium silicates formation, the latter was ascribed to alloying with lithium silicide as final product. At a more negative potential, below 0.2 V, lithium insertion into carbon occurs and overlaps with silicon lithiation. Subsequent cyclic voltammetry curves overlapped confirming reproducibility of the process. The discharge capacity of the material, after 30 charge-discharge cycles, equals to 550 mAh/g. Electrochemical impedance spectroscopy measurements, with the presence of the generalized finite-length Warburg element, evidence nonuniform diffusion in a finite-length region, typical for non-homogenous materials.

Finally, using non-flammable silica as the anodic material improves safety conditions of the device. The current density of our material is higher than commercially used graphite.

ACKNOWLEDGEMENTS

Authors gratefully acknowledge the financial support from the National Science Centre, Kraków, Poland (NN 1503/B/H03/2011/40). We are thankful to Ms. Szaniawska for silica aerogel synthesis.

References

1. B.A. Boukamp, G.A. Lesh, R.A. Huggins, *J. Electrochem. Soc*., 128 (1981) 725.
2. K. Miyachi, H. Yamamoto, H. Kawai, T. Ohta, M. Shirakata, *J. Electrochem. Soc.*, 152 (2005) 2089.
3. U. Kasavajjula, C. Wang, A.J. Appleby, *J. Power Sources*, 163 (2007) 1003.
4. H. Wu, Y. Cui, *Nano Today*, 7 (2012) 414.
5. H. Wu, G. Chan, J.W. Choi, I. Ryu, Y. Yao, M.T. McDowell, S.W. Lee, A. Jackson, Y. Yang, L. Hu, Y. Cui, *Nat. Nanotechnol.*, 7 (2012) 310.
6. Q. Sun, B. Zhang, Z.-W. Fu, *Appl. Surf. Sci*., 254 (2008) 3774.
7. N. Yan, F. Wang, H. Zhong, Y. Li, Y. Wang, L. Hu, Q. Chen, *Sci. Rep.*, 3 (2013) 1568.
8. Y. Yao, J. Zhang, L. Xue, T. Huang, A. Yu, *J. Power Sources*, 196 (2011) 10240.
9. J.-W. Song, C.C. Nguyen, S.-W. Song, *RSC Adv.*, 2 (2012) 2003.
10. I. Abrahams, P.G. Bruce, A.R. West, W.I.F. David, *J. Solid State Chem*., 75 (1988) 390.
11. A.R. West, *J. Appl. Electrochem.*, 3 (1973) 327.
12. W.-S. Chang, C.-M. Park, J.-H. Kim, Y.-U. Kim, G. Jeong, H.-J. Sohn, *Energy Environ. Sci.*, 5 (2012) 6895.
13. H.-H. Li, X.-L. Wu, H.-Z. Sun, K. Wang, C.-Y. Fan, L.-L. Zhang, F.-M. Yang, J.-P. Zhang, *J. Phys. Chem. C*, 119 (2015) 3495.
14. Y. Liang, L. Cai, L. Chen, X. Lin, R. Fu, M. Zhang, D. Wu, *Nanoscale*, 7 (2015) 3971.
15. J. Kim, D. Thien, J. Kang, S. Song, *J. Alloy Compd.*, 633 (2015) 92.
16. J.-H. Kim, S. Lee, Y.-S. Lee, *J. Ind. Eng. Chem*., (2015) 1.

17. [B. Guo, J. Shu, Z. Wang, H. Yang, L. Shi, Y. Liu, L. Chen, *Electrochem. Commun.*, 10 (2008) 1876.
18. M. Stolarski, J. Walendziewski, M. Steininger, *Appl. Catal. A Gen.*, 177 (1999) 139.
19. K. Szaniawska, M. Gładkowski, L. Wicikowski, L. Murawski, *J. Non. Cryst. Solids*, 354 (2008) 4481.
20. G.S. Kim, S.H. Hyun, *Thin Solid Films*, 460 (2004) 190.
21. J.-N. Rouzaud, C. Clinard, *Fuel Process. Technol.*, 77-78 (2002) 229.
22. R.E. Franklin, *P. Roy. Soc. A-Math. Phy.*, 209 (1951) 196.
23. S.G. Hutchison, L.S. Richardson, C.M. Wai, *Metall. Trans. B*, 19 (1988) 249.
24. M.P. Delplancke, *J. Vac. Sci. Technol. A*, 9 (1991) 450.
25. J. Lücke, J. Hacker, D. Suttor, G. Ziegler, *Appl. Organomet. Chem.*, 11 (1997) 181.
26. F. Tuinstra, J.I. Koenig, J. Chem. Phys. 53 (1970) 1126.
27. Y.-S. Hu, R. Demir-Cakan, M.-M. Titirici, J.-O. Müller, R. Schlögl, M. Antonietti, J. Maier, *Angew. Chemie Int. Ed.*, 47 (2008) 1645.
28. A.C. Ferrari, J. Robertson, *Phys. Rev. B*, 61 (2000) 14095.
29. A. Sadezky, H. Muckenhuber, H. Grothe, R. Niessner, U. Pöschl, *Carbon N. Y.*, 43 (2005) 1731.
30. Y. Wang, D.C. Alsmeyer, R.L. Mccreery, *Chem. Mater.*, (1990) 557.
31. B. Dippel, H. Jander, J. Heintzenberg, *Phys. Chem. Chem. Phys.*, 1 (1999) 4707.
32. L. Martín, J.O. Ossó, S. Ricart, A. Roig, O. García, R. Sastre, *J. Mater. Chem.*, 18 (2008) 207.
33. A. Nyczyk-Malinowska, M. Wójcik-Bania, T. Gumuła, M. Hasik, M. Cypryk, Z. Olejniczak, *J. Eur. Ceram. Soc.*, 34 (2014) 889.
34. H. El Rassy, A.C. Pierre, *J. Non. Cryst. Solids*, 351 (2005) 1603.
35. A. Avila, I. Montero, L. Galán, J.M. Ripalda, R. Levy, *J. Appl. Phys.*, 89 (2001) 212.
36. [L. Muehlhoff, W.J. Choyke, M.J. Bozack, J.T. Yates, *J. Appl. Phys.*, 60 (1986) 2842.
37. J. Kikuma, K. Yoneyama, M. Nomura, T. Konishi, T. Hashimoto, R. Mitsumoto, Y. Ohuchi, K. Seki, *J. Electron Spectros. Relat. Phenomena*, 88-91 (1998) 919.
38. R.I.R. Blyth, H. Buqa, F.P. Netzer, M.G. Ramsey, J.O. Besenhard, *Appl. Surf. Sci.*, 167 (2000) 99.
39. J. Światowska, V. Lair, C. Pereira-Nabais, G. Cote, P. Marcus, A. Chagnes, *Appl. Surf. Sci.*, 257 (2011) 9110.
40. C. Chan, R. Ruffo, S. Hong, Y. Cui, *J. Power Sources*, 189 (2009) 1132.
41. B. Philippe, J. Allouche, F. Lindgren, M. Gorgoi, D. Gonbeau, K. Edstro, *Chem. Mater.*, 24 (2012) 1107.
42. H. Nara, T. Yokoshima, M. Otaki, T. Momma, T. Osaka, *Electrochim. Acta*, 110 (2013) 403.
43. L. Chen, T. Goto, T. Hirai, T. Amano, *J. Mater. Sci. Lett.*, 9 (1990) 997.
44. Q. Xia, B. Wang, Y.P. Wu, H.J. Luo, S.Y. Zhao, T. van Ree, *J. Power Sources*, 180 (2008) 602.
45. G. Beamson, *Surf. Sci. Spectra*, 3 (1994) 357.
46. X. Liu, M.-C. Zheng, K. Xie, *J. Power Sources*, 196 (2011) 10667.
47. H. Takezawa, K. Iwamoto, S. Ito, H. Yoshizawa, *J. Power Sources*, 244 (2013) 149.
48. M. Herstedt, D.P. Abraham, J.B. Kerr, K. Edström, *Electrochim. Acta*, 49 (2004) 5097.
49. [T. Asakawa, K. Tanaka, I. Toyoshima, *Langmuir*, 4 (1988) 521.
50. C.-H. Doh, A. Veluchamy, D.-J. Lee, J.-H. Lee, B.-S. Jin, S.-I. Moon, C.-W. Park, D.-W. Kim, Bull. *Korean Chem. Soc.*, 31 (2010) 1257.
51. F. La Mantia, J. Vetter, P. Novák, *Electrochim. Acta*, 53 (2008) 4109.
52. W. Xing, *J. Electrochem. Soc.*, 144 (1997) 1195.
53. Y. Ren, H. Wei, X. Huang, J. Ding, *Int. J. Electrochem. Sci.*, 9 (2014) 7784.
54. A. Lisowska-Oleksiak, A.P. Nowak, B. Wicikowska, *RSC Adv.*, 4 (2014) 40439.
55. Y.-K. Kim, J.-W. Moon, J.-G. Lee, Y.-K. Baek, S.-H. Hong, *J. Power Sources*, 272 (2014) 689.
56. C. Gao, H. Zhao, P. Lv, C. Wang, J. Wang, T. Zhang, Q. Xia, *J. Electrochem. Soc.*, 161 (2014) A2216.

57. J. Tu, W. Wang, L. Hu, H. Zhu, S. Jiao, *J. Mater. Chem.*, A 2 (2014) 2467.
58. F. Dai, R. Yi, M.L. Gordin, S. Chen, D. Wang, *RSC Adv.*, 2 (2012) 12710.
59. H. Fukui, H. Ohsuka, T. Hino, K. Kanamura, *ACS Appl. Mater. Inter.*, 2 (2010) 998.
60. N. Liu, H. Wu, M.T. McDowell, Y. Yao, C. Wang, Y. Cui, *Nano Lett*., 12 (2012) 3315.
61. J.R. MacDonald, M.B. Johnson, Impedance Spectroscopy: Emphasizing Solid Materials and Systems, Wiley-Vch, New York, 1987.
62. C. Wang, A.J. Appleby, F.E. Little, *Electrochim. Acta*, 46 (2001) 1793.